



HAL
open science

Simulations of the upper critical solution temperature behavior of poly(ornithine-co-citrulline)s using Martini-based coarse-grained force fields

Anne-Elisabeth Molza, Ping Gao, Justine Jakpou, Julien Nicolas, Nicolas Tsapis, Tâp Ha-Duong

► **To cite this version:**

Anne-Elisabeth Molza, Ping Gao, Justine Jakpou, Julien Nicolas, Nicolas Tsapis, et al.. Simulations of the upper critical solution temperature behavior of poly(ornithine-co-citrulline)s using Martini-based coarse-grained force fields. *Journal of Chemical Theory and Computation*, 2021, 17 (7), pp.4499-4511. 10.1021/acs.jctc.1c00140 . hal-03286381

HAL Id: hal-03286381

<https://hal.science/hal-03286381>

Submitted on 14 Jul 2021

HAL is a multi-disciplinary open access archive for the deposit and dissemination of scientific research documents, whether they are published or not. The documents may come from teaching and research institutions in France or abroad, or from public or private research centers.

L'archive ouverte pluridisciplinaire **HAL**, est destinée au dépôt et à la diffusion de documents scientifiques de niveau recherche, publiés ou non, émanant des établissements d'enseignement et de recherche français ou étrangers, des laboratoires publics ou privés.

Simulations of the upper critical solution temperature behavior of poly(ornithine-co-citrulline)s using Martini-based coarse-grained force fields

Anne-Elisabeth Molza,[†] Ping Gao,[†] Justine Jakpou,[‡] Julien Nicolas,[‡] Nicolas
Tsapis,^{*,‡} and Tâp Ha-Duong^{*,†}

[†]*Université Paris-Saclay, CNRS, BioCIS, 92290, Châtenay-Malabry, France*

[‡]*Université Paris-Saclay, CNRS, Institut Galien Paris Saclay, 92290, Châtenay-Malabry,
France*

E-mail: nicolas.tsapis@universite-paris-saclay.fr; tap.ha-duong@universite-paris-saclay.fr

Phone: +33 1 46 83 58 13; +33 1 46 83 57 38

Abstract

Poly(ornithine-*co*-citrulline)s are ureido-based polymers which were shown to exhibit tunable upper critical solution temperature (UCST) behavior, a property that can be exploited to develop thermoresponsive nanoparticles for controlled drug delivery systems. To gain insight into the driving forces that govern the formation and dissolution processes of poly(ornithine-*co*-citrulline) nanoparticles, a molecular dynamics (MD) simulation study has been carried out using MARTINI-based protein coarse-grained models. Multi-microsecond simulations at temperatures ranging from 280 to 370 K show that the fully reparametrized version 3.0 of MARTINI force field is able to capture the dependence on temperature of poly(ornithine-*co*-citrulline) aggregation and

dissolution, while version 2.2 could not account for it. Furthermore, the phase separation observed in these simulations allowed to extrapolate a phase diagram based on the Flory-Huggins theory of polymer solution which could help in future rational design of drug delivery nanoparticles based on poly(amino acid)s.

1 Introduction

The use of stimuli-sensitive nanoparticles as drug delivery systems is of great interest in pharmaceutical sciences for the selective drug targeting of diseased organs. The main strategy is to encapsulate drugs into stealth nanocarriers which will distribute them through blood capillaries in the body, and then to locally apply a physical stimulus which will specifically trigger the drug release in organs needing treatment only. Drug delivery can thus be controlled by using nanoparticles responding to various stimuli such as light, magnetic field, ultrasound, or temperature.^{1,2} Among these stimuli, hyperthermia is very promising since it can be easily locally induced using several techniques including ultrasound,³ radiofrequency,⁴ light,⁵ or simply a water bath. The prerequisite for applying these techniques is to design thermoresponsive drug nanocarriers sensitive to mild hyperthermia (that is having a transition temperature in the 40-45 °C range).

Nanoparticles based on thermoresponsive polymers have been developed for this application.^{6,7} Two types of thermoresponsive polymers can be used: those which are soluble in water below a lower critical solution temperature (LCST) and insoluble above, and those which are insoluble in water below an upper critical solution temperature (UCST) and soluble above. So far, most of the thermoresponsive nanocarriers have been developed based on LCST polymers, and much less effort has been devoted to UCST counterparts.^{6,8} Yet, UCST polymers enable the development of much more efficient drug delivery systems compared to LCST nanocarriers which release drugs through polymer collapse, often leading to entrapment of part of the drugs.⁶ In contrast, UCST nanocarriers are expected to completely release their drug payloads above their transition temperature by polymer dissociation and

dissolution. Moreover, full solubility in water of UCST polymers above their critical temperature may facilitate excretion through renal filtration as compared to insoluble LCST nanoparticles. Thus, UCST polymers provide great opportunities of innovation in the field of "smart" drug delivery systems.

Yet, only a few UCST polymers with a transition temperature in water relevant for biomedical applications have been developed and used as effective thermoresponsive drug delivery systems.^{6,9} These include polymers based on *N*-acryloylglycinamide (PNAGA),^{10,11} acrylamides (notably poly(acrylamide-*co*-acrylonitrile) (PAAm)),^{9,12,13} ureido-based polymers such as poly(allylurea) (PAU),^{14,15} and imidazole-based polymers.^{16,17} However, the lack of biodegradability of most of those synthetic polymers is a major concern which must be addressed in view of bench-to-bedside translations.

In the last decade, some proteins have been shown to undergo soluble-to-insoluble phase separation *in vivo* to fulfil their biological function.^{18,19} Many of these proteins are characterized by low complexity sequences (i.e. with fewer amino acid types compared to protein average composition) or repeating patterns of short segments, and have an intrinsically disordered structure.^{18,20} It was even demonstrated that proteins composed of repeats of P-X_n-G sequences, where n varies from 0 to 4 and X is either an apolar or charged residue, exhibited tunable LCST or UCST transitions, respectively.²¹ Given their biocompatibility and biodegradability, these proteins paved the way to the design and the development of thermoresponsive drug delivery systems based on synthetic UCST poly(amino acid)s.²²

To assist chemists to rationally design new UCST polymers and physicists to characterize their self-organization properties, molecular simulation techniques can provide precious information on structures of polymer assemblies as well as on the physical forces that govern their dynamics behavior.²³⁻²⁵ Nevertheless, all-atom simulations of several polymers composed of about 100 repeat units (monomers) in explicit solvent are computationally expensive and too time consuming for exploring exhaustively their conformational space. Thus, they can hardly yield quantitative information about polymer thermodynamic equilibrium states and

a fortiori about their phase transitions. To capture the self-assembly process of several polymer chains, it is more appropriate to use coarse-grained models which typically describe a polymer repeat unit by only few beads instead of all its atoms.^{26–28} Among the most popular coarse-grained models, the MARTINI force fields were parameterized by targeting the partition free energies between water and octanol of biomolecule building blocks.^{29–35} Since self-assemblies are largely driven by hydrophobic and polar interactions, MARTINI models are particularly well suited to study these processes.

Nonetheless, among the known limitations of MARTINI models, several studies reported that MARTINI force fields tend to overestimate some inter-biomolecular interactions, leading to excessive aggregation propensity of proteins.^{36–39} Regarding the UCST polymers that we aim at studying, this shortcoming could result in incorrect simulations of polymer aggregation or dissolution upon heating. To address this concern, we conducted extensive molecular dynamics (MD) simulations of the aggregation and dissociation processes of poly(ornithine-*co*-citrulline) chains described with MARTINI models.

Poly(ornithine-*co*-citrulline)s are ureido-based polymers which were shown to exhibit tunable UCST behavior by Shimada *et al.*^{14,15,40} Ornithine and citrulline are non-proteinogenic amino acids bearing a pendant primary amine and an ureido moiety, respectively. Under physiological conditions of pH and ion concentration, ureido groups have the peculiarity of being able to form strong hydrogen bonds between them, strengthening polymer-polymer interactions. On the other hand, primary amine groups which are protonated at physiological pH, repel each other by electrostatic forces, favoring polymer dissociation. Thus, it is possible to control the transition temperature of poly(ornithine-*co*-citrulline)s by tuning the proportion of primary amines relative to ureido groups. The objective of this work is to assess the capability of MARTINI-based force fields to correctly capture the fine balance between polymer-polymer and polymer-water interactions which determine the UCST behavior of poly(ornithine-*co*-citrulline)s with the view to use them as thermoresponsive drug delivery nanoparticles.

2 Methods

2.1 MARTINI coarse-grained models

Since its first release in 2007,²⁹ the MARTINI force fields have continuously evolved to improve the agreements with experimental observations. Regarding lipids and proteins, version 2.2 was released in 2012 and a major upgrade (version 3.0) has just been published in March 2021. Thanks to the transferable building block philosophy of MARTINI force fields, we based our coarse-grained models of poly(ornithine-*co*-citrulline) on existing parameters, first, of version 2.2 and, thereafter, on the open beta version 3.0.b.3.2 available from the MARTINI web site.^{41,42} It should be noted that MARTINI coarse-grained models do not include any chirality center. Therefore, the poly(amino acid)s simulated in this study should be regarded as racemic poly(DL-ornithine-*co*-DL-citrulline)s (P_{DL}OC) with random coil conformations.⁴⁰

The coarse-grained description of ornithine and citrulline is specified in Fig. 1. As for all amino acids, their backbone atoms NH-C α H α -CO were mapped into one bead of type P5 in MARTINI 2.2 or P2 in MARTINI 3.0. Ornithine side chain can be considered as a lysine with one less carbon. Thus, its four heavy atoms can be mapped into one single bead of type Qd or Qp in version 2.2 or 3.0, respectively. It should be noted that, at physiological pH, each of the two latter grains bears one positive charge.^{43,44} Citrulline side chain is very similar to the one of arginine, except for its terminal uncharged ureido group. In MARTINI 2.2, its four heavy atoms C β , C γ , C δ , and N ϵ were mapped into one bead of type N0, and its three terminal atoms C ζ , N ω , and O ω into one bead of type P4 like uncharged arginine.³⁰ **In MARTINI 3.0, the three carbons C β , C γ , and C δ of the propane fragment are grouped into one bead of type SN2d, while the atoms of the whole ureido moiety are grouped in one bead of type SP4 (Fig. 1). This new mapping is more consistent with the guidelines of MARTINI developers which recommend to avoid dividing chemical groups between two beads.⁴²**

Regarding the bonded interactions, the parameters for the springs connecting citrulline

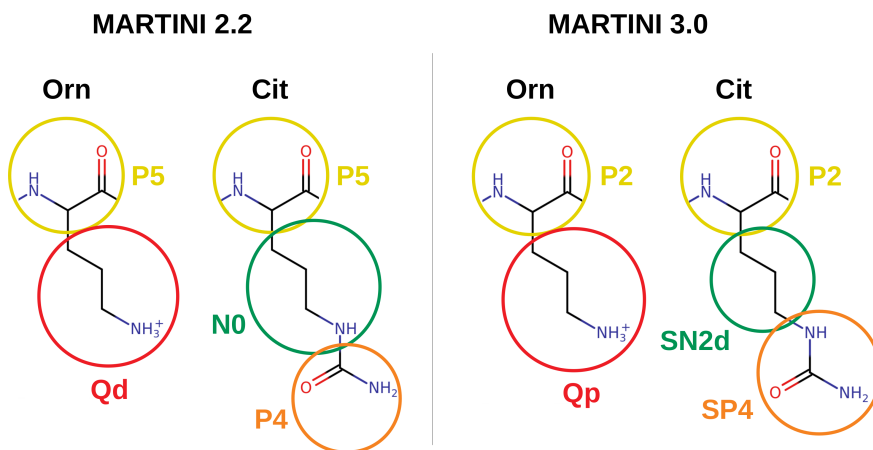


Figure 1: Mapping of amino acids ornithine and citrulline in MARTINI 2.2 (left) and MARTINI 3.0 (right) coarse-grained models. The parameters for the Lennard-Jones potentials between all the poly(ornithine-*co*-citrulline) bead types are detailed in Table S1.

coarse grains were taken from those of arginine without modification.³⁰ For ornithine, since its side chain is composed of four heavy atoms linearly connected, we used the bonded parameters of methionine (Table S2). The bonded parameters for backbone beads were taken from Ref.³⁰ for MARTINI 2.2 and Ref.⁴¹ for MARTINI 3.0. **It should be mentioned that the adoption for citrulline and ornithine side-chains of bonded parameters from similar amino acids without recalibration could induce overestimated non-bonded interactions and distort their packing in polymer aggregates.**⁴⁵ To estimate this risk, we compared the solvent accessible surface area (SASA) of isolated citrulline and ornithine in 10 ns MD simulations at the all-atom and coarse-grained levels. As displayed in Fig. S1, the amino acid SASA computed with both MARTINI models are lower than values from all-atom calculations. The largest difference is observed for the SASA of citrulline modeled with MARTINI 3.0, but the deviation remains lower than 10% of the all-atom value. This suggests that the bonded parameters adopted for citrulline and ornithine will cause minor distortions in their side chain interactions and packing.

Furthermore, with the intent of comparing random coil *versus* helical polymers, we simulated poly(ornithine-*co*-citrulline)s with add-on elastic networks between the backbone beads (but not the side chain ones) of residues that we wanted to keep in helical conformation. In

practice, we used the option *-elastic* of the *martinize* script with an upper elastic bond cutoff of 0.6 nm and a spring force constant of 500 kJ/mol/nm² (default value). Finally, it should be mentioned that the coarse-grained non-polarizable models of water, sodium, and chloride ions of each MARTINI version were used in this study. Notably, when using MARTINI 2.2, 10% of the water beads W were replaced by antifreeze particles WF to prevent freezing of the coarse-grained water.²⁹ The new non-polarizable water model WN in MARTINI 3.0 avoids the use of antifreeze particles.

2.2 Free energy calculations

Before running simulations of poly(ornithine-*co*-citrulline) aggregation, we verified the hydrophilicity character of the coarse-grained amino acids by computing their octanol-water partition coefficient $\log P_{ow}$. To this end, we employed the umbrella sampling technique⁴⁶ to calculate the octanol-water transfer free energy ΔG_{ow} of citrulline and ornithine described with MARTINI force fields. In practice, a biphasic system is built within a 24×12×12 nm³ rectangular box, half of which is filled with coarse-grained water and the other one with octanol. For each amino acid, a series of initial configurations was created by pulling the solute along a ξ axis from the center of the water phase ($\xi = 0$ nm) to the center of the octanol box ($\xi = 12$ nm) with a 0.2 nm spacing. For each solute position, which is restrained by a 1 000 kJ/mol/nm² harmonic force, the system was shortly equilibrated during 100 ps and then submitted to a 5 ns production run. The solute free energy profile along the ξ axis was retrieved by using the weighted histogram analysis method (WHAM) implemented in the GROMACS utility *gmx wham*⁴⁷ and displayed in Fig. S2.

The free energy profiles were used to calculate the octanol-water transfer free energy $\Delta G_{ow} = \Delta G_o - \Delta G_w$ and the associated partition coefficient $\log P_{ow} = -\Delta G_{ow}/(2.303RT)$ which are both reported in Table 1. It can be observed that umbrella sampling calculations generally underestimated the transfer free energies and hydrophilicities of the two amino acids when compared to experiments. The largest discrepancies are observed for the charged

ornithine calculations, irrespective of the coarse-grained force field. Regarding citrulline, the difference with experiment is decreased from 4.0 to 2.7 kJ/mol when upgrading from MARTINI 2.2 to 3.0, which can be fairly considered as acceptable. It could be noted that the transfer free energy of citrulline computed with MARTINI 3.0 remains lower than experimental measurement even though the bead type SN2d chosen for its alkane segment (based on the arginine parameterization) is usually devoted to weakly polar chemical groups. The choice of a hydrophobic SC2 bead type for this alkane moiety would probably result in a larger discrepancy.

Table 1: Comparison between umbrella sampling calculations and experimental measurements of octanol-water transfer free energy ΔG_{ow} and partition coefficient $\log P_{ow}$ of citrulline and ornithine. Experimental values of $\log P_{ow}$ were retrieved from the PubChem database.⁴⁸

	ΔG_{ow} (kJ/mol)			$\log P_{ow}$		
	MARTINI 2.2	MARTINI 3.0	Exp.	MARTINI 2.2	MARTINI 3.0	Exp.
Ornithine	19.0	17.8	24.2	-3.31	-3.10	-4.22
Citrulline	14.3	15.6	18.3	-2.49	-2.72	-3.19

Umbrella sampling simulations were also used to compute the potential of mean force (PMF) of the citrulline-citrulline and citrulline-ornithine pairs in water. In that case, two coarse-grained amino acids were placed in a cubic box of 5.3 nm side and solvated with water beads. For each pair, a serie of initial configurations was created with an intermolecular distance ξ increasing from 0.30 to 1.80 nm by an increment of 0.05 nm. Then each system was submitted to a 100 ns MD simulation with the intermolecular distance restrained by a force constant of 1 000 kJ/mol/nm². The free energy profile (PMF) for each amino acid pair was computed as a function of the distance ξ by using *gmx wham*.⁴⁷ It should be noted that restraints were applied to the distance between amino acids, but not to their positions. Thus each pair of amino acids is free to rotate. The number of rotational configurations being proportional to the surface of the sphere of radius ξ , the configuration entropy increases and the PMF decreases when ξ increases.⁴⁹ Therefore, the computed potentials of mean force were corrected by adding the term $RT\ln(4\pi\xi^2)$ to cancel out the PMF decrease and obtain a flat PMF at large separation distances ξ .

2.3 MD simulation procedures

The molecular system that serves as a benchmark for testing the ability of MARTINI models to simulate the UCST behavior of poly(ornithine-*co*-citrulline)s is composed of 24 chains at the concentration of 2.5 mM (0.031 g/mL), 150 mM of sodium chloride, and about 300 000 water beads. Each chain possesses 8 ornithine and 72 citrulline residues with random ornithine positions in the sequence. Thus, citrullines represent 90% of the sequence length, close to the ureido ratios of the L_{30K}92.4 and DL_{32K}93.5 polymers experimentally studied by Kuroyanagi *et al.*⁴⁰ It should also be noted that both N-terminal and C-terminal extremities were considered as methylated and accordingly modeled by two neutral backbone beads.

Initial pure random coil conformations of P_{DL}OC were generated using the statistical coil generator software Flexible-Meccano.⁵⁰ Conformations with helical structures at specific positions of the sequence were built by using the YASARA program⁵¹ and homemade python scripts. Then, all individual structures were converted into coarse-grained models using the *martinize.py* script.⁵² For the study of polymer aggregation process, the PACKMOL program⁵³ was used to generate starting configurations in which 24 chains were separated and randomly placed and oriented in a simulation box. Then, simulation boxes were subsequently filled with water and ion beads using GROMACS tools *gmx solvate* and *gmx genion*.

All simulations were performed with version 2018.7 of GROMACS.⁵⁴ The non-bonded cut-off scheme Verlet was used with a pair-list update periodicity of 20 steps. Lennard-Jones and Coulomb potentials and forces were shifted to zero at the cut-off distance of 1.1 nm. Short-range electrostatic interactions were screened with a relative dielectric constant $\epsilon_r = 15$ and long-range ones were treated using the reaction-field method with a relative dielectric constant $\epsilon_{rf} = \infty$.⁵⁵ Temperature and pressure were kept constant using the velocity rescaling technique⁵⁶ with the time constant $\tau_T = 1$ ps and the Parrinello–Rahman algorithm⁵⁷ with the coupling constant $\tau_P = 12$ ps, respectively. The Newton’s equations of motion were integrated using the leap-frog algorithm with a time step of 20 fs. After a minimization of 50 000 steps and an equilibration of 10 ns, each system was simulated during 7 μ s at each

studied temperature and $P = 1$ bar. MD trajectory frames were saved every 2 ps for subsequent analysis. It should be noted that, for calculating average physical quantities, only the last $5\mu\text{s}$ of the trajectories were used.

MD trajectories were analyzed using homemade routines or GROMACS tools. In particular, the polymer aggregation states were monitored using the *g_aggregates* program⁵⁸ which can compute the number of aggregates and their size as a function of time. In this study, the threshold distance used to classify two chains as part of the same aggregate is set to 0.6 nm. The *gmx_sasa* tool was used to calculate the polymer aggregate solvent accessible surface area and volumes from which the concentrations of diluted and condensed phases were determined for calculating the polymer phase diagram.

2.4 Phase diagram calculation

When a polymer solution undergoes a phase separation under some conditions, it is possible to "extrapolate" its phase diagram from the polymer concentrations in the dilute and condensed phases determined under these conditions. This calculation, described here, is based on the Flory-Huggins theory of polymer solution:^{59,60} At constant temperature and pressure, the dimensionless Gibbs free energy change for mixing a polymer with N repeating units (here, $N = 80$ residues) and a solvent for which each molecule occupies the same volume as one repeating unit is

$$g(\phi) = \frac{\Delta G_m}{k_B T} = \phi(1 - \phi)\chi + \frac{\phi}{N}\ln(\phi) + (1 - \phi)\ln(1 - \phi) \quad (1)$$

The polymer volume fraction ϕ is calculated as $\phi = c/\rho$ where c and ρ are respectively the polymer mass concentration and density. In this study, the average density of P_{DL}OC was estimated using the molecular-weight-dependent function $\rho(M)(g/mL) = 1.41 + 0.145 \times \exp(-M(kDa)/13.4)$ from Fisher *et al.*⁶¹ which yields the density $\rho = 1.47$ g/mL for a chain of 8 ornithines and 72 citrullines ($M = 12.25$ kDa).

The Flory-Huggins parameter χ describes the polymer-solvent interactions. Empirically, χ depends on the temperature as $\chi(T) = A + B/T$ where A and B are two parameters to be determined experimentally⁶² or using simulations. Indeed, if for some discrete temperatures T_i a phase separation is observed, then the Flory-Huggins parameters χ_i can be calculated from the polymer volume fractions in dilute (ϕ_d^i) and condensed (ϕ_c^i) phases and the equality of the chemical potentials μ_d and μ_c of the two phases in equilibrium:

$$\begin{aligned} \mu_d = \mu_c &\iff g'(\phi_d^i) = g'(\phi_c^i) \iff \\ (1 - 2\phi_d^i)\chi_i + \frac{1}{N}\ln\phi_d^i - \ln(1 - \phi_d^i) &= (1 - 2\phi_c^i)\chi_i + \frac{1}{N}\ln\phi_c^i - \ln(1 - \phi_c^i) \\ \implies \chi_i &= [\frac{1}{N}\ln(\frac{\phi_c^i}{\phi_d^i}) - \ln(\frac{1-\phi_c^i}{1-\phi_d^i})]/[2(\phi_c^i - \phi_d^i)] \end{aligned} \quad (2)$$

Thus, using a linear regression of data points $(\chi_i, 1/T_i)$, we can determine the two parameters A and B of the Flory-Huggins parameter for the studied polymer and solvent. Subsequently, knowing the function $\chi(T) = A + B/T$, the dimensionless Gibbs free energy can be calculated at any temperature for all polymer volume fraction ϕ .

At a given temperature, if the curve of function $g(\phi)$ has a local concave curvature, then the derivative function $g'(\phi)$ is non-monotonic and there are two different volume fractions ϕ_d and ϕ_c for which the chemical potentials are equal, indicating a possible phase separation (Fig. 2).⁶³ The concave curvature of $g(\phi)$ also implies the existence of two volume fractions ϕ_{s1} and ϕ_{s2} , called spinodal points, such as $g''(\phi_{s1}) = g''(\phi_{s2}) = 0$.⁶⁴ A polymer solution with an initial volume fraction ϕ_0 between ϕ_{s1} and ϕ_{s2} will phase separate into two coexisting phases with $\phi_d < \phi_{s1}$ and $\phi_{s2} < \phi_c$.⁶³

However, the equality of chemical potentials $g'(\phi_d) = g'(\phi_c)$ is not sufficient to determine ϕ_d and ϕ_c . A second condition is that the free energy of the two coexisting phases $g_0 = \lambda g(\phi_d) + (1 - \lambda)g(\phi_c)$, where λ is the fraction of polymers in diluted phase, must be minimum. Since $\phi_0 = \lambda\phi_d + (1 - \lambda)\phi_c$, we can write that $\phi_d = \phi_0 - (1 - \lambda)\Delta\phi$ and $\phi_c = \phi_0 + \lambda\Delta\phi$,

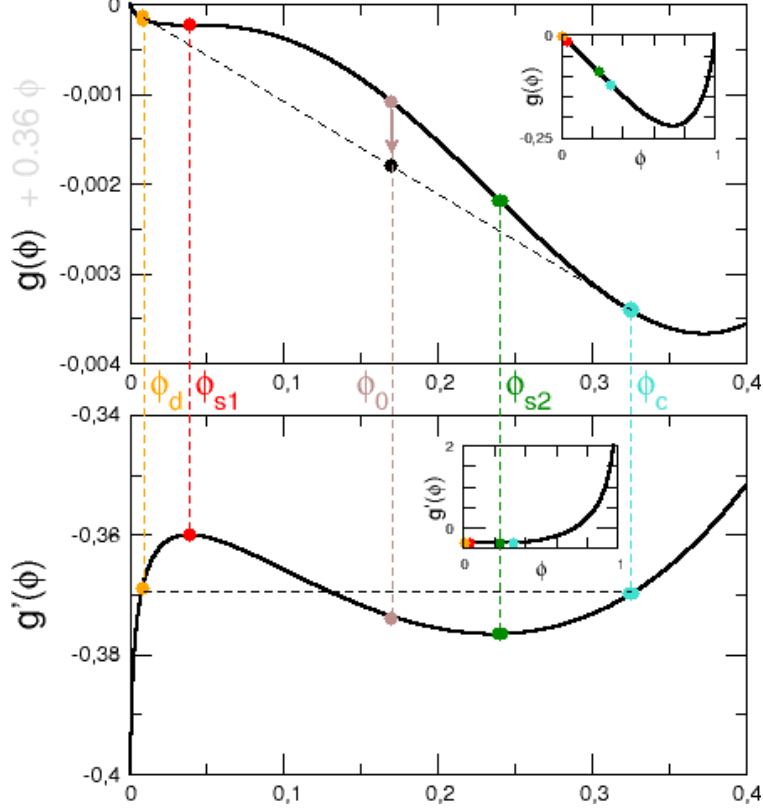


Figure 2: Curves of dimensionless functions $g(\phi)$ (top) and $g'(\phi)$ (bottom) obtained from Eq. (1) with parameters $N = 80$ and $\chi = 0.68$. In the top graph, the function $g(\phi) + 0.36\phi$ is plotted to accentuate the concave curvature of $g(\phi)$ which is less visible without this artefact. The unaltered curves are displayed in the inset graphs. The red and green points are the two spinodal points for which $g''(\phi_{s1}) = g''(\phi_{s2}) = 0$. The brown point represents a polymer solution with an initial volume fraction ϕ_0 which will separate into two phases represented by orange and cyan points and characterized by the volume fractions ϕ_d and ϕ_c , respectively.

where $\Delta\phi = \phi_c - \phi_d$, and it appears that g_0 is a function of λ :

$$g_0(\lambda) = \lambda g(\phi_0 - (1 - \lambda)\Delta\phi) + (1 - \lambda)g(\phi_0 + \lambda\Delta\phi) \quad (3)$$

At the minimum of $g_0(\lambda)$, the condition $g'_0(\lambda) = 0$ leads to $g(\phi_d) + \lambda\Delta\phi g'(\phi_d) - g(\phi_c) + (1 - \lambda)\Delta\phi g'(\phi_c) = 0$. Since $g'(\phi_d) = g'(\phi_c)$, this yields the relation $g(\phi_d) - \phi_d g'(\phi_d) = g(\phi_c) - \phi_c g'(\phi_c)$. Graphically, this means that the tangents to the curve $g(\phi)$ at the points ϕ_d and ϕ_c are the same (Fig. 2). In conclusion, for a polymer solution demixing into two phases,

the dilute and condensed volume fractions can be determined using the two conditions:

$$g'(\phi_d) = g'(\phi_c) \tag{4}$$

$$g(\phi_d) - \phi_d g'(\phi_d) = g(\phi_c) - \phi_c g'(\phi_c) \tag{5}$$

There is no simple analytical solution of these two equations. But it is possible to determine ϕ_d and ϕ_c using numerical methods, such as the one described in Supporting Information.

3 Results

3.1 Simulations with MARTINI 2.2

At the start of this study, we wished to ascertain whether random coil poly(DL-ornithine-*co*-DL-citrulline) (P_{DL}OC) described with MARTINI 2.2 force field exhibited a UCST behavior in MD simulations. To this end, we simulated the aggregation process of 24 chains, initially separated, at the temperatures of 280, 310, and 370 K. As displayed in the left column of Fig. 3, when the citrulline ureido group has the default type P4 (Fig.1), the 24 chains rapidly aggregates into one cluster at all temperatures, even before the end of equilibration runs at 280 and 370 K. Clearly, no temperature effect is observed with this bead type.

Since polymer UCST property is generally related to a fine balance between polymer-polymer and polymer-solvent interactions, we attempted to improve the P_{DL}OC coarse-grained model by deepening the Lennard-Jones potential of citrulline ureido bead from type P4 ($\epsilon_{LJ} = 5.0$ kJ/mol) to P5 ($\epsilon_{LJ} = 5.6$ kJ/mol).²⁹ We even tested an original bead type P6 ($\epsilon_{LJ} = 6.0$ kJ/mol) not present in MARTINI 2.2. As observed in Fig. 3, the ureido bead type P5 induces more fluctuations in the polymer aggregation state, but no UCST behavior could be detected, since large polymer aggregates are observed at all temperatures (Fig. 3 and Table S3). Unexpectedly, bead type P6 did not improve the model but yielded similar results as with type P4.

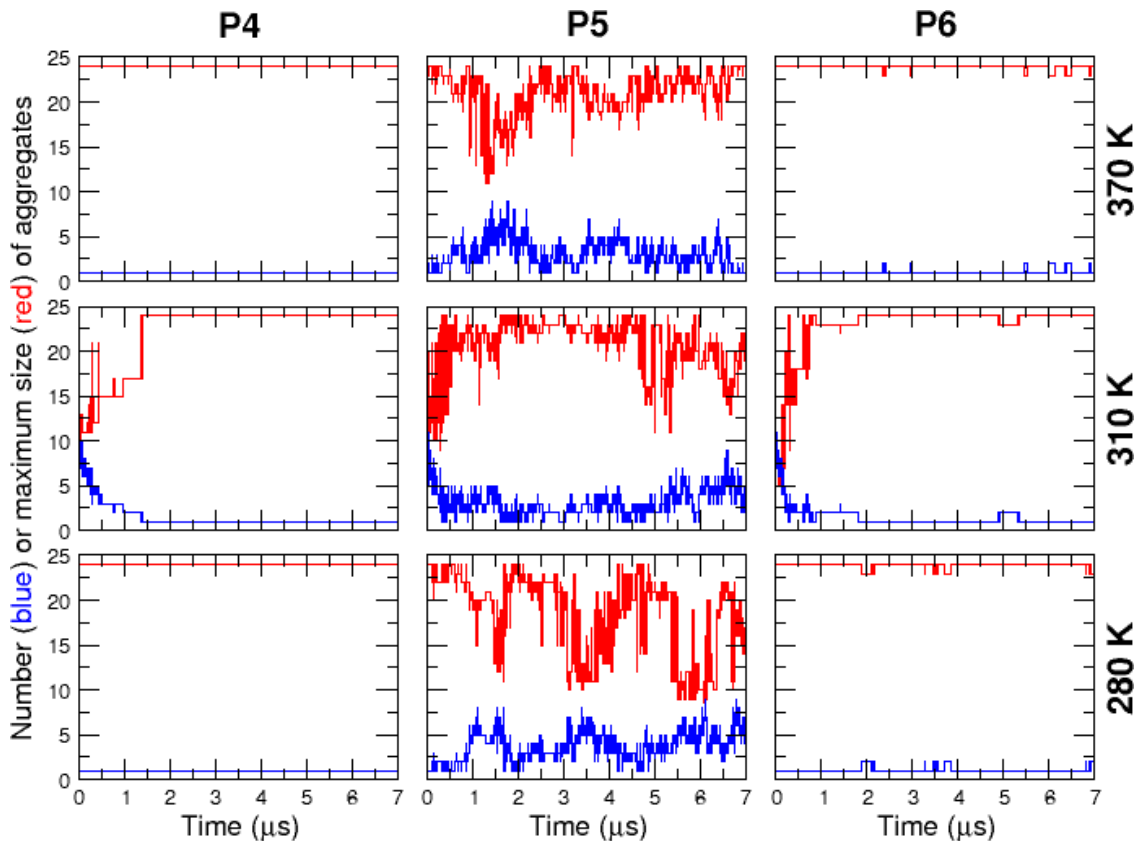


Figure 3: Influence of the citrulline ureido bead type on the aggregation of $P_{\text{DL}}\text{OC}$ random coil chains at 280, 310, 370 K (from bottom to top rows). Left, middle, and right columns show results for MARTINI 2.2 type P4, P5, and P6, respectively. Blue and red lines indicate the number of aggregates and the number of chains in the largest aggregate, respectively.

When using type P5 for the citrulline ureido bead, a possible explanation for the absence of UCST behavior is the weakness of the repulsive forces between the ornithine charged side chains. To test this hypothesis, we run simulations of the $P_{\text{DL}}\text{OC}$ aggregation with decreased values of the solvent dielectric constant which screens the electrostatic interactions. However, for both values $\epsilon_r = 5$ and $\epsilon_r = 10$, instead of the default $\epsilon_r = 15$, the polymer aggregation behavior does not seem to rationally respond to temperature (Fig. S4 and Table S4 of Supporting Information). Altogether, in line with previously observed stickiness of protein models based on MARTINI 2.2,^{36–39} our simulations with this force field were not able to reproduce the dissolution of $P_{\text{DL}}\text{OC}$ in water at high temperature. Our attempts to improve the model with small modifications were unfruitful and probably disrupted the co-

herence of the force field.⁴⁵ We thus decided to switch to the fully reparametrized MARTINI version 3.0.b.3.2.^{41,65}

3.2 Simulations with MARTINI 3.0

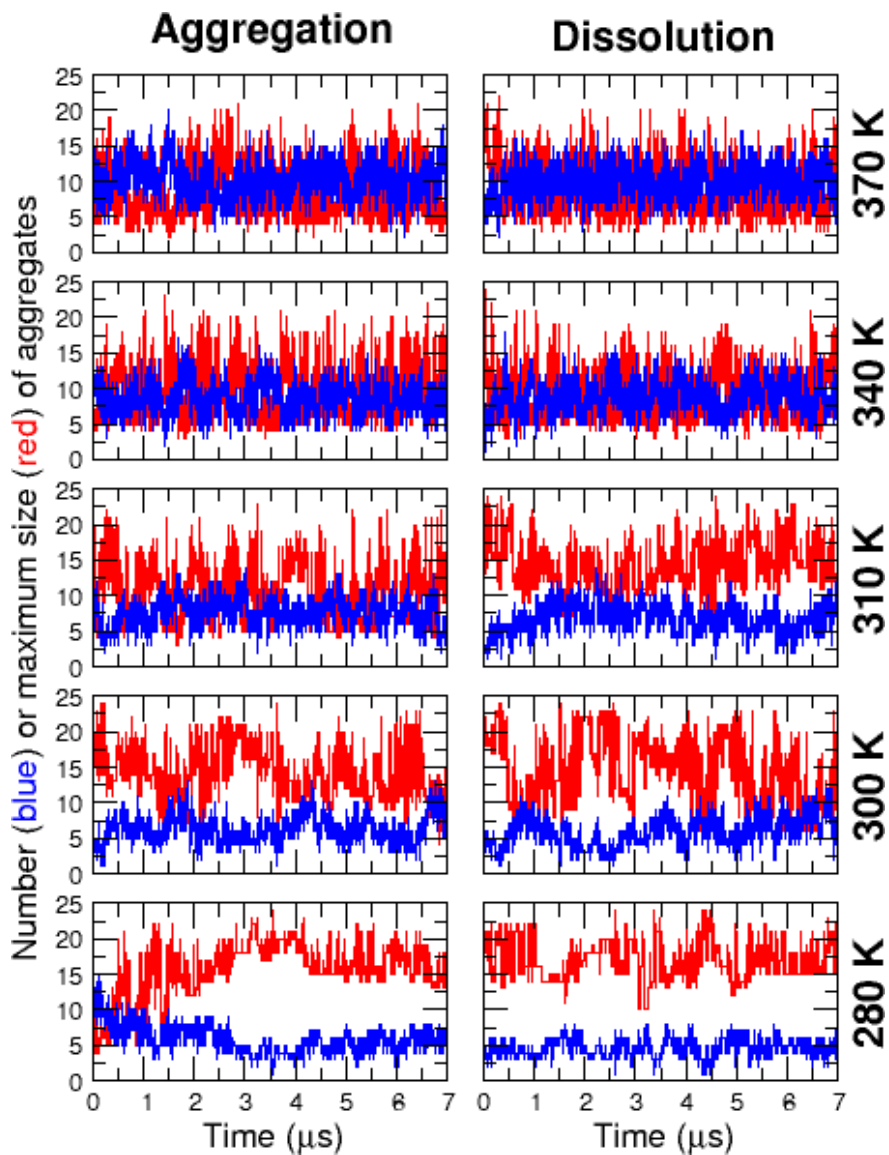


Figure 4: Simulation with MARTINI 3.0 of the aggregation (left column) and dissolution (right column) of P_{DL}OC random coil chains at 280, 300, 310, 340, and 370 K (from bottom to top rows). Blue and red lines indicate the number of aggregates and the number of chains in the largest aggregate, respectively.

In contrast to results obtained with MARTINI 2.2, a clear effect of temperature on the

aggregation of P_{DL}OC could be observed by using the new MARTINI force field (Fig. 4). Starting from separated chains, the aggregation process is quite slow at 280 K and reaches an equilibrium after about 3 μ s, whereas aggregation already occurred during the equilibration steps at 300 and 310 K. Importantly, at high temperatures (340 and 370 K), no formation of large aggregations could be observed. To confirm the UCST behavior of P_{DL}OC in our simulations with MARTINI 3.0, we extracted an aggregate of 24 chains from the aggregation trajectory at 280 K (at time $t = 3547$ ns) and defined it as the starting point for simulations of the dissolution process as a function of temperature. As displayed in right column of Fig. 4, the aggregate rapidly dissolves in water at 340 and 370 K but remains more and more stable when decreasing temperature.

To quantitatively measure the influence of temperature upon polymer aggregation states at equilibrium, the distributions of the number of aggregates and of the size of the largest one were computed over the last 5 μ s of both aggregation and dissolution simulations. As seen in Fig. 5 and Table S5, the average number of aggregates and the size of the largest one increases and decreases upon heating, respectively. Distributions of the biggest aggregate size have a larger width at 300 and 310 K than at the other temperatures, suggesting that phase transition between dissolved and aggregated states occurs around these temperatures. It could be noted that the term "dissolved state" may be improperly used here since none of the systems showed monodisperse polymers completely isolated and aggregates continuously form and split, even at high temperature. Given the small number of chains in our simulated systems, we can intuitively consider that the polymers are in a dissolved state when more than half of them are not assembled in the largest aggregate. Conversely, polymers are in an aggregated state when more than 50% of them are assembled in the largest aggregate.

This being said, a definite delimitation between dissolved and aggregated states can be obtained by determining the temperature of transition between the two phases. To this end, the average number of aggregates and the average number of chains that are not in the largest one were plotted as a function of the temperature and fitted with a sigmoidal curve

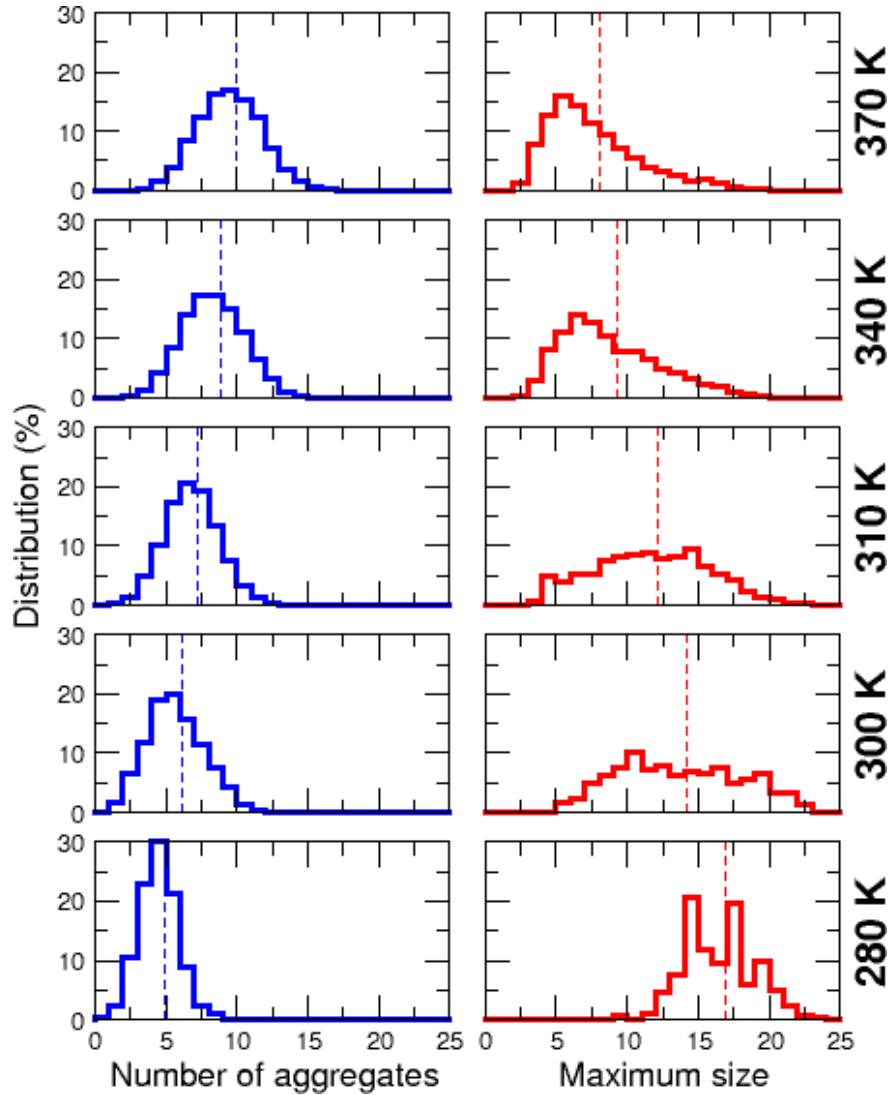


Figure 5: Distributions of the number of aggregates (left column) and of the size of the largest one (right column) computed over aggregation and dissolution simulations of $P_{DL}OC$ at the five studied temperatures. Vertical dashed lines indicate average values.

characteristic of phase transitions. The latter parameter which is the complementary of the size of the largest aggregate was considered just by convenience because it exhibits a growing curve with temperature like experimental transmittance measurements of UCST polymers.⁴⁰ As shown in Fig. 6, one can discern an increase of these numbers at low temperature followed by a saturation at high temperature. Both sets of data can be very well fitted with sigmoidal functions $y(x) = a0/[1 + \exp(-a1(x - a2))]$ with very close values for parameter $a2$ which indicates a phase transition temperature at 288 K.

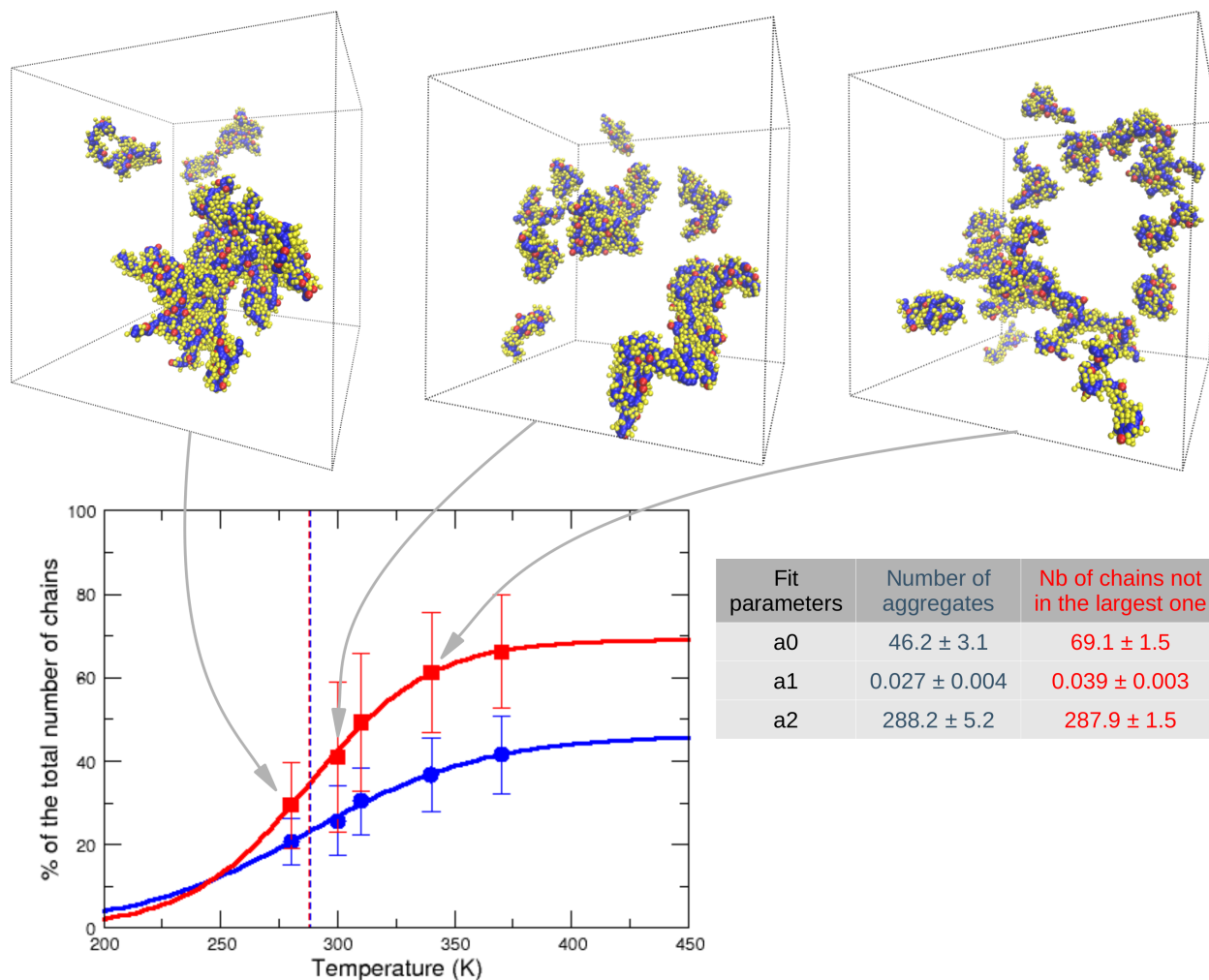


Figure 6: Temperature dependence of the average percentages of number of aggregates (blue circles) and of number of chains that are not in the largest one (red squares) in simulations of random coil P_{DL}OC. Solid lines represent sigmoidal functions $y(x) = a0/[1 + \exp(-a1(x - a2))]$ that fit data from simulations (weighted by $1/\sigma_i^2$, where σ_i is the standard deviation of each point). Fit parameters and their standard error (bottom right table) were obtained by using the *optimize.curve_fit* function from the python module *SciPy*.⁶⁶ Vertical dashed line indicates the transition temperature found by the two fitting curves. Representative snapshots of P_{DL}OC aggregation states are displayed for the three temperatures 280, 300, and 340 K. Blue, yellow, and red balls indicate backbone beads, citrulline side chains, and ornithine side chains, respectively.

3.3 Polymer aggregation as a function of their helical content

In their recent experimental study of poly(ornithine-*co*-citrulline) UCST properties, Kuroyanagi *et al.* demonstrated that racemic and homochiral chains had different phase separation behaviors.⁴⁰ The authors showed that solubilized racemic P_{DL}OC possess random coil con-

formations and form liquid droplets upon cooling below their transition temperature. In contrast, solubilized homochiral poly(L-ornithine-*co*-L-citrulline)s (P_LOC) are structured in α -helices and aggregate into solid hexagonal packings below critical temperature.

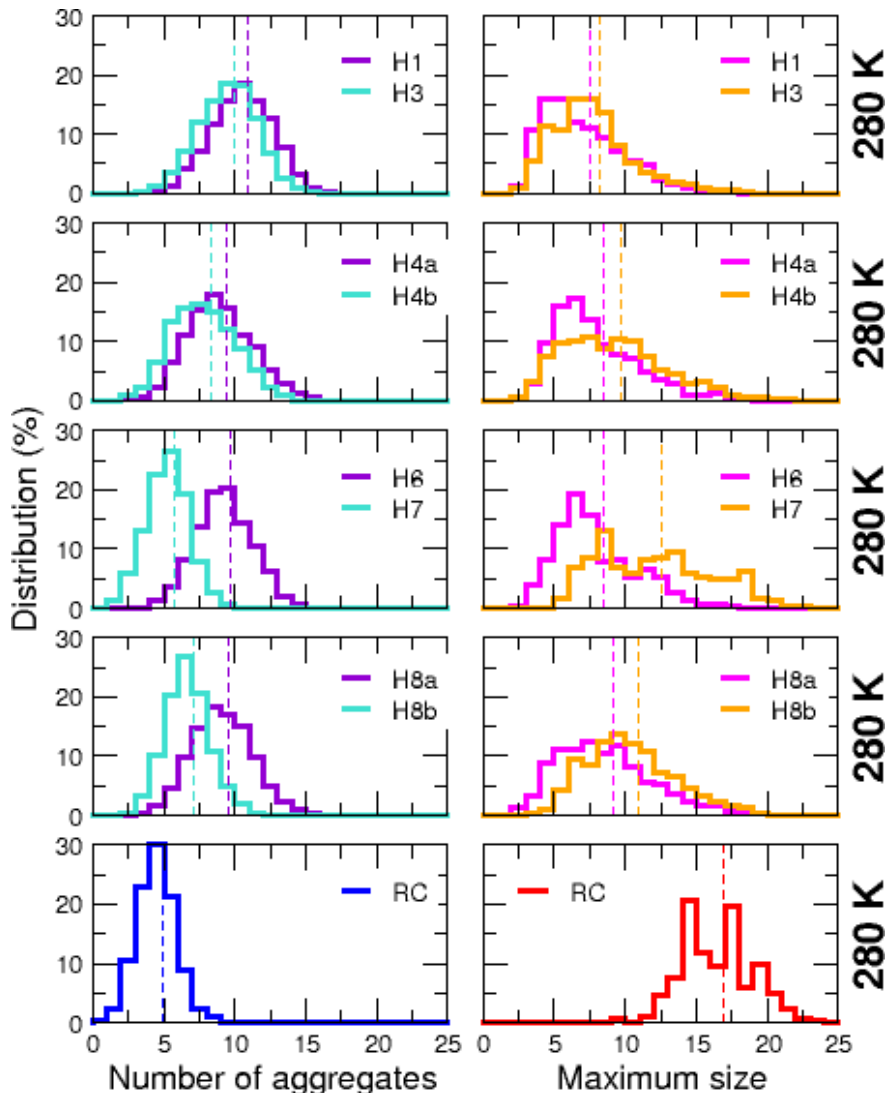


Figure 7: Distributions of the number of aggregates (left column) and of the size of the largest one (right column) computed over the last 5 μ s of helical P_LOC simulations at 280 K. H1, H3, H4a, H4b, H6, H7, H8a, H8b chains contain 1 helix of 72 residues, 3 helices of 24 residues, 4 helices of 18 residues, 4 helices of 16 residues, 6 helices of 10 residues, 7 helices of 8 residues, 8 helices of 8 residues, and 8 helices of 6 residues, respectively. Data for random coil P_{DL}OC simulations are recalled in the bottom row for comparison. Vertical dashed lines indicate average values.

Unfortunately, coarse-grained models of poly(ornithine-*co*-citrulline)s cannot account for chirality of amino acids. However, using elastic networks, it is possible to impose helical

conformations to specific segments of coarse-grained polymers. Thus, using MD simulations at low temperature (280 K), we investigated here the effect of P_LOC helical patterns on their aggregation process to compare with that of random coil chains. We considered 8 different polymer systems of 24 initially separated chains (each of them being composed of 72 citrullines and 8 ornithines randomly located in the sequence). In each system, all polymers have the same helical pattern which is 1 helix of 72 residues (H1), 3 helices of 24 residues (H3), 4 helices of 18 residues (H4a), 4 helices of 16 residues (H4b), 6 helices of 10 residues (H6), 7 helices of 8 residues (H7), 8 helices of 8 residues (H8a), or 8 helices of 6 residues (H8b). Helices are connected by 4 residues in random coil conformation, except in systems with 4 helices of 18 residues or 8 helices of 8 residues whose linkers are composed of only 2 random coil residues (see top of graphs in Fig. S5).

MD simulations with MARTINI 3.0 show that P_LOC with long helical segments (longer than 10 residues) do not form stable large aggregates. In contrast, polymers with shorter helices (less than 8 residues) can assemble into larger aggregates (Fig. S5 and Table S6). However, it seems that the length of the random coil segments connecting the helices is also important. Indeed, P_LOC chains with helices connected by only 2 random coil residues are less prone to form large aggregates than polymers with the same number of helices but connected by 4 random coil residues. The helical polymer system which exhibits the highest propensity to aggregate is composed of chains with 7 helices of 8 residues. However, when we compare the maximal size of the aggregates for helical P_LOC *versus* random coil P_{DL}OC (Fig. 7), it can be observed that the distribution is wider and the average is lower for H7 than for random coil polymers, suggesting that aggregates of H7 chains seem less stable than those of random coil at 280 K. In addition, a visual inspection of the MD trajectory of H7 chains could not allow to identify hexagonal packing of P_LOC helices as experimentally observed by Kuroyanagi *et al.*⁴⁰ This indicates that simulations did not reach the equilibrium aggregation states of helical P_LOC chains.

Nevertheless, we still wanted to study the effect of polymer helicity upon their UCST

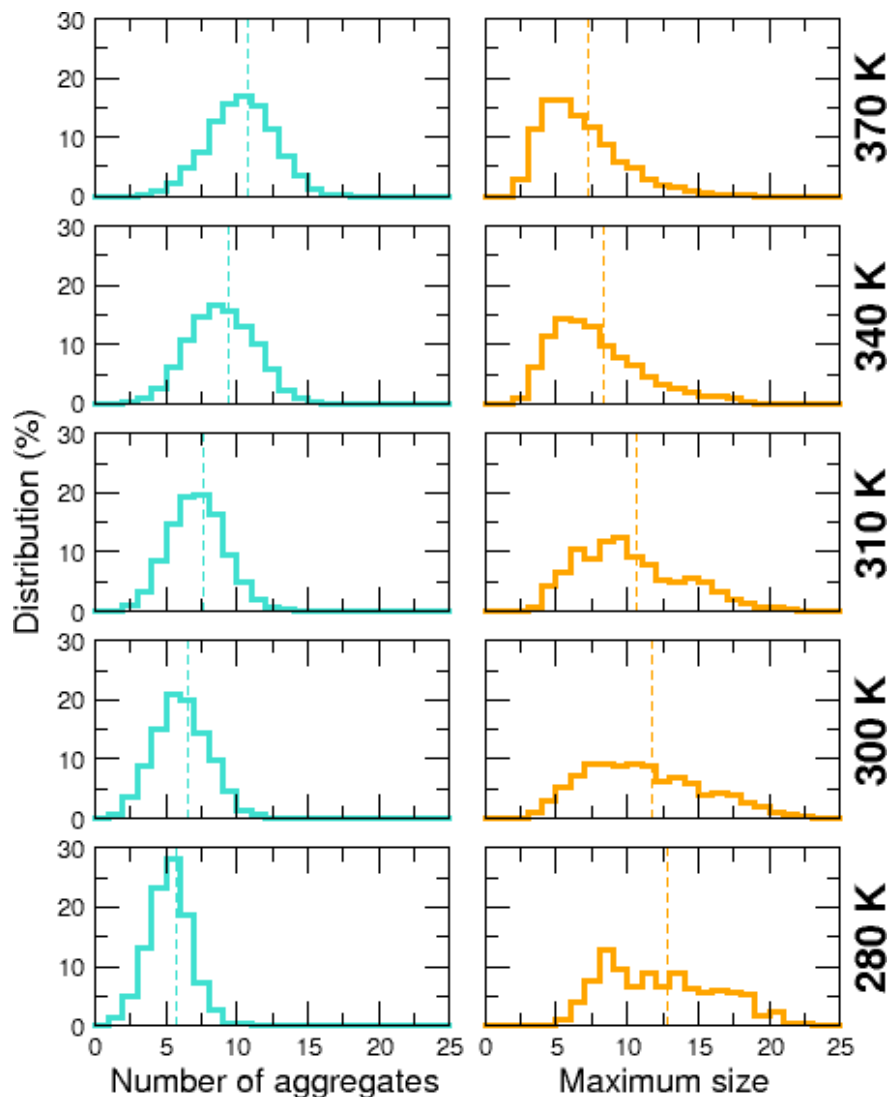


Figure 8: Distributions of the number of aggregates (left column) and of the size of the largest one (right column) computed over the last 5 μ s of both aggregation and dissolution simulations of P_LOC chains with 7 helices of 8 residues (H7) at the five studied temperatures. Vertical dashed lines indicate average values.

property. Thus, we simulated the influence of temperature upon the aggregation and dissolution of P_LOC chains composed of 7 helical segments of 8 residues. As displayed in Fig. 8, these helical polymers also exhibit a slight UCST property: Simulations generated polymer aggregates of decreasing size when temperature increases from 280 to 370 K (Table S7). However, when the average number of aggregates and the average number of chains that are not in the largest one are plotted as a function of the temperature and fitted with sigmoidal

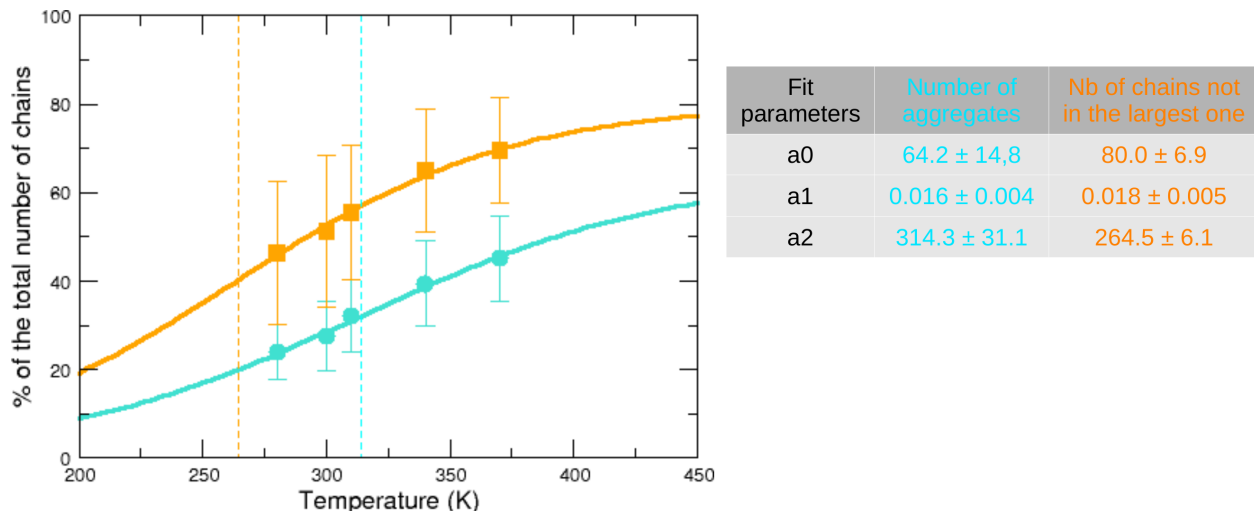


Figure 9: Temperature dependence of the average percentages of number of aggregates (cyan circles) and of number of chains that are not in the largest one (orange squares) in simulations of P_LOC chains with 7 helices of 8 residues (H7). Solid lines represent sigmoidal functions $y(x) = a0/[1+exp(-a1(x-a2))]$ that fit data from simulations (weighted by $1/\sigma_i^2$, where σ_i is the standard deviation of each point). Fit parameters and their standard error (right table) were obtained by using the *optimize.curve_fit* function from the python module *SciPy*.⁶⁶ Vertical dashed line indicates the transition temperature found by the two fitting curves.

curves (Fig. 9), the phase transition appears less sharp than for random coil P_{DL}OC. Moreover, unlike what was observed for random coil chains (Fig. 6), the two fitting functions did not yield the same value for the transition temperature (299 K for the number of aggregates and 266 K for the number of polymers not in the largest aggregate). This did not allow to unambiguously determine a theoretical transition temperature that could be compared to experimental measurement. Again, we could not obtain conclusive results for this system, and for this reason, we did not calculate the phase diagram of helical P_LOC.

3.4 Polymer phase diagram

From the P_{DL}OC aggregates observed in MD simulations at low temperatures (280-310 K), it is possible to calculate the concentration of dilute and condensed phases under these conditions and then to extrapolate the polymer phase diagram using the Flory-Huggins theory.^{59,60} The concentration of the condensed phase was calculated by considering that it is composed of aggregates with at least 12 chains, which is about the average size of

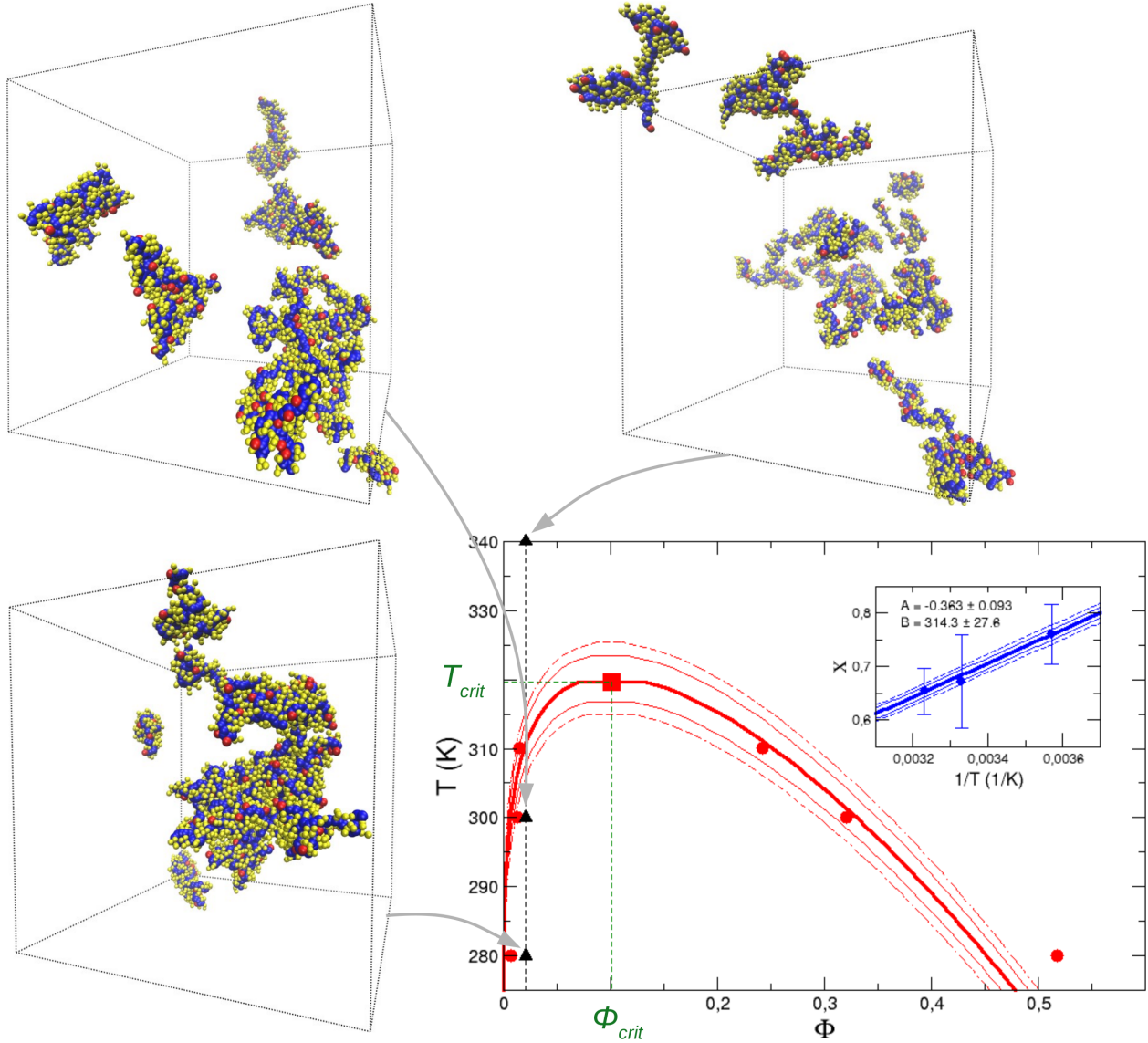


Figure 10: Temperature *versus* volume fraction phase diagram of P_{DLOc} calculated using the Flory-Huggins theory. Red circles represent temperatures and volume fractions calculated from MD simulations. Red square is the critical temperature and volume fraction predicted by the Flory-Huggins theory (also indicated by green dashed lines). Black dashed line represents the volume fraction of MD simulations. The inset graph displays the Flory-Huggins parameter χ as a function of $1/T$. Blue circles are data calculated from MD simulations and solid line represents the linear function $\chi(T) = A + B/T$ that fit the data weighted by $1/\sigma_i^2$, where σ_i is the standard deviation of each point (Table S8). The fit parameters A and B and their standard errors were obtained by using the *optimize.curve_fit* function of python module *SciPy*.⁶⁶ The thin solid and dashed lines represent the $\chi(T)$ functions and coexistence curves obtained with the four extreme symmetric values of parameters (A , B) for which it is possible to calculate a phase diagram.

the largest aggregates at 310 K (Fig. 5), a temperature around which the phase transition occurred. The volume of these aggregates was estimated by using the GROMACS tools *gmx sasa* with a solvent probe radius of 0.26 nm which is the Lennard-Jones radius of MARTINI water beads.⁶⁷ The volume of the dilute phase is calculated by subtracting the volume of the condensed phase from the simulation box volume. Finally, the concentrations and volume fractions ϕ_d and ϕ_c of the dilute and condensed phases were calculated from their computed volumes and averaged over the last 5 μ s of each trajectory.

P_{DL}OC phase separation occurred only at low temperatures 280, 300, and 310 K. Therefore, only data from simulations at these three temperatures were used to estimate the polymer phase diagram. Using the volume fractions ϕ_d and ϕ_c of the dilute and condensed phases calculated from MD trajectories, the Flory-Huggins parameter χ can be estimated at these temperatures. Then a linear regression of the three points allows to determine the two parameters A and B of the function $\chi(T) = A + B/T$ (see inset graph of Fig. 10).

The two regression parameters A and B are then input in the algorithm described in Supporting Information to compute the coexistence curve that delineates the conditions for which two phases can be observed (under the bell-curves) from those for which the polymers are in only one phase (Fig. 10). As expected from the Flory-Huggins theory, this curve is asymmetrical and sharply increases when ϕ increases from 0 to the critical volume fraction $\phi_{crit} = (1 + \sqrt{N})^{-1} = 0.101$. At this point, the critical Flory-Huggins parameter is $\chi_{crit} = 0.5 \times (1 + 1/\sqrt{N})^2 = 0.618$, and the critical temperature T_{crit} , also referred to as UCST, is equal to 320 K. For a polymer concentration of 1 mg/mL corresponding to a volume fraction of $\phi = 0.0007$, the temperature transition is estimated at 282 K in agreement with experimental measurements on similar systems.⁴⁰

To provide an approximate uncertainty on the computed phase diagram, we proceeded as follows: For parameter A fixed to its mean value ($A = -0.363$), B is increased (and decreased) by an increment of one unit from its mean value until no phase diagram could be computed. Similarly, for parameter B fixed to its mean value ($B = 314.3$), A is increased

(and decreased) by an increment of 0.002 from its mean value, until no phase diagram could be computed. This way, we obtained four extreme symmetric values of parameters (A, B) for which it is possible to calculate a phase diagram: $(-0.363, 309.3)$, $(-0.363, 319.3)$, $(-0.373, 314.3)$, and $(-0.353, 314.3)$. The associated functions $\chi(T)$ and phase diagrams are plotted in Fig. 10. The critical temperatures found with these for couples of parameters are 314.9, 325.4, 316.8, and 323.5 K, respectively, indicating that the uncertainty on the polymer UCST (320 K) is about 5 K.

4 Discussion

We reported here a study on the ability of MARTINI coarse-grained force fields to model the UCST behavior of poly(ornithine-*co*-citrulline)s. To this end, we performed MD simulations of 24 initially separated random coil P_{DL}OC chains and monitored their aggregation process at five temperatures from 280 to 370 K. In simulations with MARTINI 2.2, heating had no effect upon the formation of polymer aggregates which occurred at all temperatures. Using MARTINI version 3.0.b.3.2, P_{DL}OC chains could aggregate at low temperatures (280, 300, and 310 K) but not at higher ones (340 and 370 K). The polymers are no longer too sticky and fluctuations of their aggregation states can be observed regardless of temperature.

These results should be explained by different balances between polymer-polymer and polymer-water interactions in the MARTINI 2.2 and MARTINI 3.0 models. To provide more in-depth analyses on the modeled water-mediated polymer-polymer interactions, we computed the citrulline-citrulline and citrulline-ornithine potentials of mean force (PMF) and compared the results yielded by the two force fields. As shown in Fig. 11, the Lennard-Jones potentials of MARTINI 2.2 result in deeper and longer range PMF than those yielded by MARTINI 3.0. This is particular noticeable for the citrulline-citrulline pair which requires 1.5 kJ/mol to be separated with MARTINI 2.2 instead of 1.0 kJ/mol with MARTINI 3.0 at low temperature. Moreover, in contrast to the other three PMF calculations, citrulline-

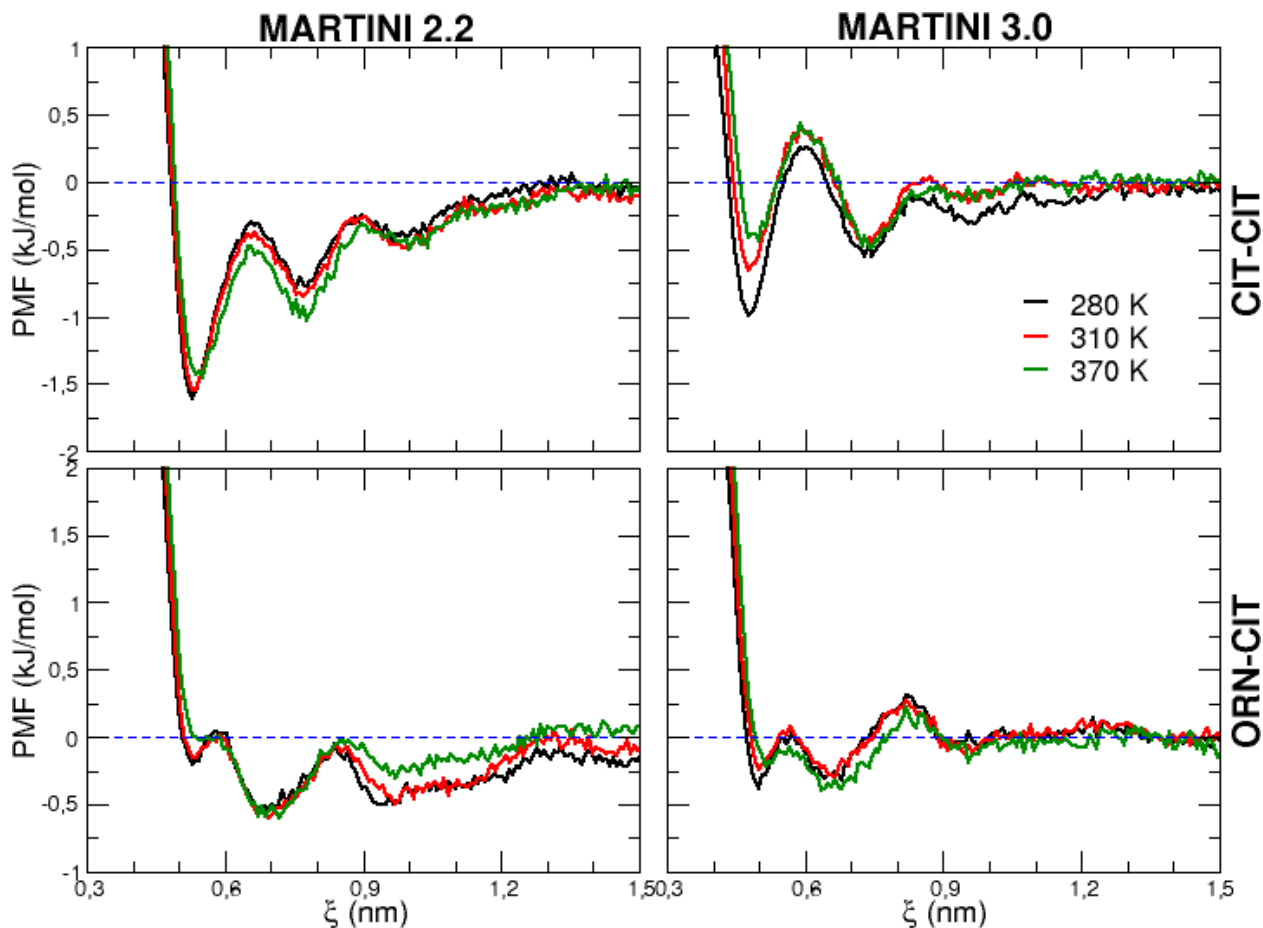


Figure 11: Potential of mean force (PMF) between two citrulline amino acids (top row) and between one citrulline and one ornithine (bottom row). The PMF were computed by using either the MARTINI 2.2 (left column) or MARTINI 3.0 (right column) force field, at temperatures 280, 310, and 370 K.


citrulline PMF computed with MARTINI 3.0 is more sensitive to temperature, since the energy cost to separate two citrullines is reduced to 0.5 kJ/mol at high temperature. Altogether, these potentials of mean force confirm that polymer models with MARTINI 2.2 are too sticky and explain why simulations with this force field generated very stable aggregates at all temperatures. In contrast, PMF generated with MARTINI 3.0 are less deep and citrulline-citrulline interactions more sensitive to temperature, accounting for the UCST property of $P_{DL}OC$ polymers.

We also investigated the influence of the polymer helical content upon their aggregation property. Starting from 24 initially separated $P_L OC$ chains with various patterns of α -helices

maintained by elastic networks, no clear phase separation was observed at 280 K, except for polymers composed of no less than 7 helical regions connected by flexible linkers of at least 4 residues in random coil. It appears that helical P_LOC chains can self-assemble provided that they have a sufficient number of linkers of at least 4 random coil residues, probably to be sufficiently flexible in order to "catch" a neighbouring chain. However, our simulations did not reach the formation of hexagonal packing of P_LOC helices as reported by Kuroyanagi *et al.*⁴⁰ This might be due to a characteristic time of forming highly ordered solid from solubilized polymers which is probably much longer than the duration of the simulations presented herein. Also, inaccuracy in the coarse-grained amino acid side chain SASA and volume could prevent an optimal hexagonal packing of the helical chains. Finally, the lack of global electric dipole in the coarse-grained models of the α -helices could also explain that anti-parallel helix-helix structures are not stabilized in simulations.

Nevertheless, P_LOC chains composed of 7 helical segments exhibit a slight and smooth UCST property in our simulations. But contrary to random coil chains, the two metrics used to monitor the helical polymer phase transition (the number of aggregates and the number of polymers not in the largest one) did not yield the same transition temperature. To better understand this difference, we analyzed the average size of the "small aggregates", i.e. the average number n_s of chains per aggregate excluding the largest one. Indeed, the latter links the number of polymer chains that are not in the largest aggregate (n_b) to the number of aggregates (n_a) as: $n_b = (n_a - 1) \times n_s$. When the size of the largest aggregate decreases upon heating, meaning that n_b increases, the number of aggregates n_a also increases (Figs. 6 and 9). But the average number n_s of polymer chains per small aggregate has a different behavior for random coils than for helical chains (Fig. S7): n_s remains rather constant in random coil systems, meaning that the chains, which unbind the largest aggregate upon heating, form new small aggregates of the same size as existing ones. In contrast, n_s decreases in helical systems, meaning that both the largest and the smaller aggregates lose some chains upon heating. In the first case, it results that the two functions $n_b(T)$ and $n_a(T)$ have a similar

temperature of transition. In the second one, $n_b(T)$ has a lower transition temperature than $n_a(T)$.

The two different transition temperatures identified in the case of helical polymers were not expected since both the number of aggregates and the size of the largest one are two metrics related to the transmittance of a polymer solution measured in experiments.⁴⁰ Thus the two transition temperatures should be in principle very close. We are convinced that our simulations of helical chains did not succeed in retrieving this unique transition temperature because helix-helix interactions were not sufficiently attractive to drive the formation of stable hexagonal packing at low temperatures, as discussed above. Otherwise, the size of the largest aggregate would be significantly larger and the number of chains not assembled to it would be much lower, particularly at 280 K. This would result in a transition curve with a transition temperature higher than 266 K and closer to the transition temperature obtained from the number of aggregates (299 K).  Further investigations and developments are certainly required to better reproduce the helix-helix interactions in hexagonal packing.

5 Conclusion

Our theoretical study shows that MARTINI 3.0.b.3.2 force field clearly improves the fine balance between the polymer-polymer and polymer-water interactions, notably by decreasing the size of citrulline side chain beads which lower the energy barrier of their association/dissociation.⁴⁵ These improvements now allow to qualitatively reproduce the UCST behavior of random coil P_{DL}OC. Nonetheless, their phase transition temperature seems to be too low (around 300 K) for using them in thermoresponsive drug delivery systems. The next stage of our research project will be to investigate whether PEGylated poly(ornithine-*co*-citrulline)s can form more stable aggregates at low temperature with a sharp phase transition temperature above 320 K in the perspective of biomedical applications.

Acknowledgement

This work was supported by the French Agence Nationale de la Recherche (grant ANR-18-CE09-0024-01). MD simulations were performed using HPC resources from GENCI-IDRIS (grant A0070710968). The authors would like to warmly thank Paulo C.T. Souza and Tsjerk A. Wassenaar for their helpful expertise in MARTINI force field developments and for the fruitful discussions about the beta version 3.0.b.3.2.

Supporting Information Available

Supporting information available online includes the parameters for the coarse-grained models of poly(ornithine-*co*-citrulline)s, the numerical method used for calculating the polymer phase diagram, the aggregation processes of P_{DL}OC as a function of the solvent dielectric constant, of P_LOC as a function of their helical content, and of P_LOC with 7 helical segments (H7) as a function of the temperature.

References

- (1) Mura, S.; Nicolas, J.; Couvreur, P. Stimuli-responsive nanocarriers for drug delivery. *Nature Materials* **2013**, *12*, 991–1003.
- (2) Lakshmanan, S.; Gupta, G. K.; Avci, P.; Chandran, R.; Sadasivam, M.; Jorge, A. E. S.; Hamblin, M. R. Physical energy for drug delivery; poration, concentration and activation. *Advanced Drug Delivery Reviews* **2014**, *71*, 98–114.
- (3) Boissenot, T.; Bordat, A.; Larrat, B.; Varna, M.; Chacun, H.; Paci, A.; Poinsignon, V.; Fattal, E.; Tsapis, N. Ultrasound-induced mild hyperthermia improves the anticancer efficacy of both Taxol® and paclitaxel-loaded nanocapsules. *Journal of Controlled Release* **2017**, *264*, 219–227.

- (4) Wu, X.; Zhang, F.; Hu, P.; Chen, L.; Han, G.; Bai, W.; Luo, J.; Chen, R.; Zhou, Y.; Sun, J.; Yang, X. Radiofrequency heat-enhanced direct intratumoral chemotherapy for prostate cancer. *Oncology Letters* **2017**, *14*, 7250–7256.
- (5) Morales-Dalmau, J.; Vilches, C.; Miguel, I. d.; Sanz, V.; Quidant, R. Optimum morphology of gold nanorods for light-induced hyperthermia. *Nanoscale* **2018**, *10*, 2632–2638.
- (6) Bordat, A.; Boissenot, T.; Nicolas, J.; Tsapis, N. Thermoresponsive polymer nanocarriers for biomedical applications. *Advanced Drug Delivery Reviews* **2019**, *138*, 167–192.
- (7) Doberenz, F.; Zeng, K.; Willems, C.; Zhang, K.; Groth, T. Thermoresponsive polymers and their biomedical application in tissue engineering – a review. *Journal of Materials Chemistry B* **2020**, *8*, 607–628.
- (8) Karimi, M.; Sahandi Zangabad, P.; Ghasemi, A.; Amiri, M.; Bahrami, M.; Malekzad, H.; Ghahramanzadeh Asl, H.; Mahdieh, Z.; Bozorgomid, M.; Ghasemi, A.; Rahmani Taji Boyuk, M. R.; Hamblin, M. R. Temperature-Responsive Smart Nanocarriers for Delivery Of Therapeutic Agents: Applications and Recent Advances. *ACS Applied Materials & Interfaces* **2016**, *8*, 21107–21133.
- (9) Seuring, J.; Agarwal, S. First Example of a Universal and Cost-Effective Approach: Polymers with Tunable Upper Critical Solution Temperature in Water and Electrolyte Solution. *Macromolecules* **2012**, *45*, 3910–3918.
- (10) Seuring, J.; Agarwal, S. Non-Ionic Homo- and Copolymers with H-Donor and H-Acceptor Units with an UCST in Water. *Macromolecular Chemistry and Physics* **2010**, *211*, 2109–2117.
- (11) Glatzel, S.; Laschewsky, A.; Lutz, J.-F. Well-Defined Uncharged Polymers with a Sharp UCST in Water and in Physiological Milieu. *Macromolecules* **2011**, *44*.

- (12) Li, W.; Huang, L.; Ying, X.; Jian, Y.; Hong, Y.; Hu, F.; Du, Y. Antitumor Drug Delivery Modulated by A Polymeric Micelle with an Upper Critical Solution Temperature. *Angewandte Chemie International Edition* **2015**, *54*, 3126–3131.
- (13) Bordat, A.; Soliman, N.; Ben Chraït, I.; Manerlax, K.; Yagoubi, N.; Boissenot, T.; Nicolas, J.; Tsapis, N. The crucial role of macromolecular engineering, drug encapsulation and dilution on the thermoresponsiveness of UCST diblock copolymer nanoparticles used for hyperthermia. *European Journal of Pharmaceutics and Biopharmaceutics* **2019**, *142*, 281–290.
- (14) Shimada, N.; Ino, H.; Maie, K.; Nakayama, M.; Kano, A.; Maruyama, A. Ureido-Derivatized Polymers Based on Both Poly(allylurea) and Poly(L-citrulline) Exhibit UCST-Type Phase Transition Behavior under Physiologically Relevant Conditions. *Biomacromolecules* **2011**, *12*, 3418–3422.
- (15) Shimada, N.; Nakayama, M.; Kano, A.; Maruyama, A. Design of UCST Polymers for Chilling Capture of Proteins. *Biomacromolecules* **2013**, *14*, 1452–1457.
- (16) Meiswinkel, G.; Ritter, H. A New Type of Thermoresponsive Copolymer with UCST-Type Transitions in Water: Poly(N-vinylimidazole-co-1-vinyl-2-(hydroxymethyl)imidazole). *Macromolecular Rapid Communications* **2013**, *34*, 1026–1031.
- (17) Zhang, G.; Wang, Y.; Liu, G. Poly(3-imidazolyl-2-hydroxypropyl methacrylate) – a new polymer with a tunable upper critical solution temperature in water. *Polymer Chemistry* **2016**, *7*, 6645–6654.
- (18) Weber, S.; Brangwynne, C. Getting RNA and Protein in Phase. *Cell* **2012**, *149*, 1188–1191.
- (19) Aguzzi, A.; Altmeyer, M. Phase Separation: Linking Cellular Compartmentalization to Disease. *Trends in Cell Biology* **2016**, *26*, 547–558.

- (20) Holehouse, A. S. *Intrinsically Disordered Proteins*; Elsevier, 2019; pp 209–255.
- (21) Quiroz, F. G.; Chilkoti, A. Sequence heuristics to encode phase behaviour in intrinsically disordered protein polymers. *Nature Materials* **2015**, *14*, 1164–1171.
- (22) Xu, H.; Yao, Q.; Cai, C.; Gou, J.; Zhang, Y.; Zhong, H.; Tang, X. Amphiphilic poly(amino acid) based micelles applied to drug delivery: The in vitro and in vivo challenges and the corresponding potential strategies. *Journal of Controlled Release* **2015**, *199*, 84–97.
- (23) Bochicchio, D.; Salvalaglio, M.; Pavan, G. M. Into the Dynamics of a Supramolecular Polymer at Submolecular Resolution. *Nature Communications* **2017**, *8*, 147.
- (24) Frederix, P. W. J. M.; Patmanidis, I.; Marrink, S. J. Molecular simulations of self-assembling bio-inspired supramolecular systems and their connection to experiments. *Chemical Society Reviews* **2018**, *47*, 3470–3489.
- (25) Gartner, T. E.; Jayaraman, A. Modeling and Simulations of Polymers: A Roadmap. *Macromolecules* **2019**, *52*, 755–786.
- (26) Kmiecik, S.; Gront, D.; Kolinski, M.; Wieteska, L.; Dawid, A. E.; Kolinski, A. Coarse-Grained Protein Models and Their Applications. *Chemical Reviews* **2016**, *116*, 7898–7936.
- (27) Pak, A. J.; Voth, G. A. Advances in coarse-grained modeling of macromolecular complexes. *Current Opinion in Structural Biology* **2018**, *52*, 119–126.
- (28) Singh, N.; Li, W. Recent Advances in Coarse-Grained Models for Biomolecules and Their Applications. *International Journal of Molecular Sciences* **2019**, *20*, 3774.
- (29) Marrink, S. J.; Risselada, H. J.; Yefimov, S.; Tieleman, D. P.; de Vries, A. H. The MARTINI Force Field: Coarse Grained Model for Biomolecular Simulations. *Journal of Physical Chemistry B* **2007**, *111*, 7812–7824.

- (30) Monticelli, L.; Kandasamy, S. K.; Periolo, X.; Larson, R. G.; Tieleman, D. P.; Marrink, S.-J. The MARTINI Coarse-Grained Force Field: Extension to Proteins. *Journal of Chemical Theory and Computation* **2008**, *4*, 819–834.
- (31) López, C. A.; Rzepiela, A. J.; de Vries, A. H.; Dijkhuizen, L.; Hünenberger, P. H.; Marrink, S. J. Martini Coarse-Grained Force Field: Extension to Carbohydrates. *Journal of Chemical Theory and Computation* **2009**, *5*, 3195–3210.
- (32) Uusitalo, J. J.; Ingólfsson, H. I.; Akhshi, P.; Tieleman, D. P.; Marrink, S. J. Martini Coarse-Grained Force Field: Extension to DNA. *Journal of Chemical Theory and Computation* **2015**, *11*, 3932–3945.
- (33) Panizon, E.; Bochicchio, D.; Monticelli, L.; Rossi, G. MARTINI Coarse-Grained Models of Polyethylene and Polypropylene. *Journal of Physical Chemistry B* **2015**, *119*, 8209–8216.
- (34) Uusitalo, J. J.; Ingólfsson, H. I.; Marrink, S. J.; Faustino, I. Martini Coarse-Grained Force Field: Extension to RNA. *Biophysical Journal* **2017**, *113*, 246–256.
- (35) Grunewald, F.; Rossi, G.; de Vries, A. H.; Marrink, S. J.; Monticelli, L. Transferable MARTINI Model of Poly(ethylene Oxide). *The Journal of Physical Chemistry B* **2018**, *122*, 7436–7449.
- (36) Stark, A. C.; Andrews, C. T.; Elcock, A. H. Toward Optimized Potential Functions for Protein–Protein Interactions in Aqueous Solutions: Osmotic Second Virial Coefficient Calculations Using the MARTINI Coarse-Grained Force Field. *Journal of Chemical Theory and Computation* **2013**, *9*, 4176–4185.
- (37) Nishizawa, M.; Nishizawa, K. Potential of mean force analysis of the self-association of leucine-rich transmembrane α -helices: Difference between atomistic and coarse-grained simulations. *Journal of Chemical Physics* **2014**, *141*, 075101.

- (38) Javanainen, M.; Martinez-Seara, H.; Vattulainen, I. Excessive aggregation of membrane proteins in the Martini model. *PLOS ONE* **2017**, *12*, e0187936.
- (39) Periolo, X.; Zeppelin, T.; Schjøtt, B. Dimer Interface of the Human Serotonin Transporter and Effect of the Membrane Composition. *Scientific Reports* **2018**, *8*, 5080.
- (40) Kuroyanagi, S.; Shimada, N.; Fujii, S.; Furuta, T.; Harada, A.; Sakurai, K.; Maruyama, A. Highly Ordered Polypeptide with UCST Phase Separation Behavior. *Journal of the American Chemical Society* **2019**, *141*, 1261–1268.
- (41) Marrink, S.; et al., Martini 3.0 Open Beta Version. <http://cgmartini.nl/index.php/force-field-parameters/particle-definitions> **2020**,
- (42) Souza, P. C. T.; Alessandri, R.; Barnoud, J.; Thallmair, S.; Faustino, I.; Grünewald, F.; Patmanidis, I.; Abdizadeh, H.; Bruininks, B. M. H.; Wassenaar, T. A.; Kroon, P. C.; Melcr, J.; Nieto, V.; Corradi, V.; Khan, H. M.; Domański, J.; Javanainen, M.; Martinez-Seara, H.; Reuter, N.; Best, R. B.; Vattulainen, I.; Monticelli, L.; Periolo, X.; Tieleman, D. P.; de Vries, A. H.; Marrink, S. J. Martini 3: a general purpose force field for coarse-grained molecular dynamics. *Nature Methods* **2021**, 1–7.
- (43) Goldsmith, J. O.; Lee, S.; Zambidis, I.; Kuo, L. C. Control of L-ornithine specificity in *Escherichia coli* ornithine transcarbamoylase. Site-directed mutagenic and pH studies. *Journal of Biological Chemistry* **1991**, *266*, 18626–18634.
- (44) Makowska, J.; Bagińska, K.; Liwo, A.; Chmurzyński, L.; Scheraga, H. A. Acidic-basic properties of three alanine-based peptides containing acidic and basic side chains: Comparison between theory and experiment. *Biopolymers* **2008**, *90*, 724–732.
- (45) Alessandri, R.; Souza, P. C. T.; Thallmair, S.; Melo, M. N.; de Vries, A. H.; Marrink, S. J. Pitfalls of the Martini Model. *Journal of Chemical Theory and Computation* **2019**, *15*, 5448–5460.

- (46) Kästner, J. Umbrella sampling. *WIREs Computational Molecular Science* **2011**, *1*, 932–942.
- (47) Hub, J. S.; de Groot, B. L.; van der Spoel, D. g-wham—A Free Weighted Histogram Analysis Implementation Including Robust Error and Autocorrelation Estimates. *Journal of Chemical Theory and Computation* **2010**, *6*, 3713–3720.
- (48) Kim, S.; Chen, J.; Cheng, T.; Gindulyte, A.; He, J.; He, S.; Li, Q.; Shoemaker, B. A.; Thiessen, P. A.; Yu, B.; Zaslavsky, L.; Zhang, J.; Bolton, E. E. PubChem in 2021: new data content and improved web interfaces. *Nucleic Acids Research* **2021**, *49*, D1388–D1395.
- (49) Neumann, R. M. Entropic approach to Brownian movement. *American Journal of Physics* **1980**, *48*, 354–357.
- (50) Ozenne, V.; Bauer, F.; Salmon, L.; Huang, J.; Jensen, M.; Segard, S.; Bernadó, P.; Charavay, C.; Blackledge, M. Flexible-meccano: a tool for the generation of explicit ensemble descriptions of intrinsically disordered proteins and their associated experimental observables. *Bioinformatics* **2012**, *28*, 1463–1470.
- (51) Krieger, E.; Vriend, G. YASARA View—molecular graphics for all devices—from smartphones to workstations. *Bioinformatics* **2014**, *30*, 2981–2982.
- (52) de Jong, D. H.; Singh, G.; Bennett, W. F. D.; Arnarez, C.; Wassenaar, T. A.; Schäfer, L. V.; Periole, X.; Tieleman, D. P.; Marrink, S. J. Improved Parameters for the Martini Coarse-Grained Protein Force Field. *Journal of Chemical Theory and Computation* **2013**, *9*, 687–697.
- (53) Martínez, L.; Andrade, R.; Birgin, E. G.; Martínez, J. M. PACKMOL: A package for building initial configurations for molecular dynamics simulations. *Journal of Computational Chemistry* **2009**, *30*, 2157–2164.

- (54) Abraham, M. J.; Murtola, T.; Schulz, R.; Páll, S.; Smith, J. C.; Hess, B.; Lindahl, E. GROMACS: High performance molecular simulations through multi-level parallelism from laptops to supercomputers. *SoftwareX* **2015**, *1–2*, 19–25.
- (55) de Jong, D. H.; Baoukina, S.; Ingólfsson, H. I.; Marrink, S. J. Martini straight: Boosting performance using a shorter cutoff and GPUs. *Computer Physics Communications* **2016**, *199*, 1–7.
- (56) Bussi, G.; Donadio, D.; Parrinello, M. Canonical sampling through velocity rescaling. *Journal of Chemical Physics* **2007**, *126*, 014101.
- (57) Parrinello, M.; Rahman, A. Polymorphic transitions in single crystals: A new molecular dynamics method. *Journal of Applied Physics* **1981**, *52*, 7182–7190.
- (58) Barnoud, J.; Rossi, G.; Monticelli, L. Lipid membranes as solvents for carbon nanoparticles. *Physical Review Letters* **2014**, *112*, 068102.
- (59) Flory, P. J. Thermodynamics of High Polymer Solutions. *Journal of Chemical Physics* **1941**, *9*, 660–660.
- (60) Huggins, M. L. Thermodynamics Properties of solutions of long-chain compounds. *Annals of the New York Academy of Sciences* **1942**, *43*, 1–32.
- (61) Fischer, H.; Polikarpov, I.; Craievich, A. F. Average protein density is a molecular-weight-dependent function. *Protein Science* **2009**, *13*, 2825–2828.
- (62) Huggins, M. L. Theory of Solutions of High Polymers. *Journal of the American Chemical Society* **1942**, *64*, 1712–1719.
- (63) Hyman, A. A.; Weber, C. A.; Jülicher, F. Liquid-Liquid Phase Separation in Biology. *Annual Review of Cell and Developmental Biology* **2014**, *30*, 39–58.

- (64) Lin, Y.-H.; Song, J.; Forman-Kay, J. D.; Chan, H. S. Random-phase-approximation theory for sequence-dependent, biologically functional liquid-liquid phase separation of intrinsically disordered proteins. *Journal of Molecular Liquids* **2017**, *228*, 176–193.
- (65) Souza, P. C. T.; Thallmair, S.; Marrink, S. J.; Mera-Adasme, R. An Allosteric Pathway in Copper, Zinc Superoxide Dismutase Unravels the Molecular Mechanism of the G93A Amyotrophic Lateral Sclerosis-Linked Mutation. *The Journal of Physical Chemistry Letters* **2019**, *10*, 7740–7744.
- (66) Virtanen, P.; Gommers, R.; Oliphant, T. E.; Haberland, M.; Reddy, T.; Cournapeau, D.; Burovski, E.; Peterson, P.; Weckesser, W.; Bright, J.; van der Walt, S. J.; Brett, M.; Wilson, J.; Millman, K. J.; Mayorov, N.; Nelson, A. R. J.; Jones, E.; Kern, R.; Larson, E.; Carey, C. J.; Polat, İ.; Feng, Y.; Moore, E. W.; VanderPlas, J.; Laxalde, D.; Perktold, J.; Cimrman, R.; Henriksen, I.; Quintero, E. A.; Harris, C. R.; Archibald, A. M.; Ribeiro, A. H.; Pedregosa, F.; van Mulbregt, P.; SciPy 1.0 Contributors, SciPy 1.0: Fundamental Algorithms for Scientific Computing in Python. *Nature Methods* **2020**, *17*, 261–272.
- (67) Periolo, X.; Knepp, A. M.; Sakmar, T. P.; Marrink, S. J.; Huber, T. Structural Determinants of the Supramolecular Organization of G Protein-Coupled Receptors in Bilayers. *Journal of the American Chemical Society* **2012**, *134*, 10959–10965.

Graphical TOC Entry

